catalysts

MDPI

Article

Ex-Situ Electrochemical Characterization of IrO_2 Synthesized by a Modified Adams Fusion Method for the Oxygen Evolution Reaction

Cecil Felix [1,*], Bernard J. Bladergroen [1], Vladimir Linkov [1], Bruno G. Pollet [1,2] and Sivakumar Pasupathi [1]

1 South African Institute for Advanced Materials Chemistry (SAIAMC), University of the Western Cape, Robert Sobukwe Road, Bellville, Cape Town 7535, South Africa; bbladergroen@uwc.ac.za (B.J.B.); vlinkov@uwc.ac.za (V.L.); bruno.g.pollet@ntnu.no (B.G.P.); spasupathi@uwc.ac.za (S.P.)

2 Hydrogen Energy and Sonochemistry Research Group, Department of Energy and Process Engineering, Faculty of Engineering, Norwegian University of Science and Technology (NTNU), NO-7491 Trondheim, Norway

* Correspondence: cecilfelix09@gmail.com; Tel.: +27-21-9599310

Received: 12 February 2019; Accepted: 19 March 2019; Published: 1 April 2019

Abstract: The development of highly stable and active electrocatalysts for the oxygen evolution reaction (OER) has attracted significant research interest. IrO_2 is known to show good stability during the OER however it is not known to be the most active. Thus, significant research has been dedicated to enhance the activity of IrO_2 toward the OER. In this study, IrO_2 catalysts were synthesized using a modified Adams fusion method. The Adams fusion method is simple and is shown to directly produce nano-sized metal oxides. The effect of the Ir precursor salt to the $NaNO_3$ ratio and the fusion temperature on the OER activity of the synthesized IrO_2 electrocatalysts, was investigated. The OER activity and durability of the IrO_2 electrocatalysts were evaluated ex-situ via cyclic voltammetry (CV), chronopotentiometry (CP), electrochemical impedance spectroscopy (EIS) and linear sweep voltammetry (LSV). Physical properties of the IrO_2 electrocatalysts were evaluated via X-ray diffraction (XRD), transmission electron microscopy (TEM), thermal gravimetric analysis (TGA), differential thermal analysis (DTA), and energy dispersive spectroscopy (EDS). The results show that the addition of excess $NaNO_3$ during the modified Adams fusion reaction is not a requirement and that higher synthesis temperatures results in IrO_2 electrocatalysts with larger particle sizes and reduced electrocatalytic activity.

Keywords: polymer electrolyte membrane water electrolyzer (PEMWE); IrO_2 electrocatalyst; modified Adams fusion method; oxygen evolution reaction

1. Introduction

The increasing need for green energy alternatives has directed the interest of many researchers towards polymer electrolyte membrane water electrolyzers (PEMWE) since this technology is able to produce high purity hydrogen, an ideal alternative energy carrier suitable to be used for providing clean electricity. Moreover PEMWE can be coupled with other renewable energy sources such as wind and solar cells [1]. However hydrogen does not exist in its molecular state in nature and has to be produced from hydrogen containing resources (e.g., water, fossil fuels etc.) [2].

Currently about 96% of hydrogen is produced by using fossil fuels as a raw material [3] while only about 4% is produced through water electrolysis due to its higher cost [4]. The main drawback of PEMWE at present is still the high cost associated with components such as the expensive precious metal electrocatalysts and the proton conducting membrane [5,6]. In an attempt to reduce the cost of the PEMWE electrocatalysts, significant research has been aimed at improving the specific performance and

durability of the electrocatalysts which would in turn facilitate a reduction in the electrocatalyst loading requirement. The oxygen evolution reaction (OER) takes place at the anode and exhibits the highest overpotential (η) of the system at typical operating current density [7]. Thus, the anode electrocatalyst has received the most research attention. Like for the oxygen reduction reaction (ORR) in proton exchange membrane fuel cells (PEMFC), the OER is kinetically sluggish as it is thermodynamically and kinetically unfavourable to remove four electrons to form the oxygen-oxygen bond [2]. IrO_2, amongst other metal oxides, shows the second-best activity with good durability whereas RuO_2 shows the best activity with poor durability [8,9]. Various methods have been considered to produce metal oxides such as the molten salt method [10], the metal organic chemical vapour deposition method [11], the sulphite complex route method [12], the sol-gel method [13], the modified polyol method [14], the hydrothermal method [8] and the Adams fusion method [15–18]. Each method has been shown to successfully synthesize nano-sized metal oxides. However, some of these methods involve steps requiring complex equipment and can thus be a technical and economical stumbling block for the upscaling process. In this study, IrO_2 was synthesized using a modified Adams fusion method as this method is relatively simple and directly produces nano-sized particles. The Adams fusion method, first described by Adams and Shriner [19], entails the fusion of the metal chloride precursor with $NaNO_3$ in air at elevated temperatures. The suggested chemical reactions that occur during a modified Adams fusion method for IrO_2 synthesis are as follows [1,20]:

$$H_2IrCl_6 + 6NaNO_3 \rightarrow 6NaCl + Ir(NO_3)_4 + 2HNO_3 \quad (1)$$

$$Ir(NO_3)_4 \rightarrow IrO_2 + 4NO_2 + O_2 \quad (2)$$

As the interest of the South African research group is to upscale the production of IrO_2, great attention was paid to the ratio of the Ir precursor salt ($H_2IrCl_6 \cdot xH_2O$) to $NaNO_3$ as well as the reaction temperature during synthesis. The electrocatalytic activity and durability were evaluated ex-situ via electrochemical techniques while X-ray diffraction (XRD), transmission electron microscopy (TEM), thermal gravimetric analysis (TGA), differential thermal analysis (DTA) and energy dispersive spectroscopy (EDS) were used for physical characterization.

2. Results and Discussion

2.1. Physical Characterization

Figure 1 shows the XRD patterns of the *as*-prepared IrO_2 and commercial IrO_2 samples. The *as*-prepared samples were labelled such that IH denotes *"in-house"* synthesized, IrO_2 is the sample type, 350 °C and 400 °C are the synthesis temperatures and 1:3, 1:10 and 1:28 are the $H_2IrCl_6 \cdot xH_2O$ to $NaNO_3$ mass ratio. Figure 1a is a 3-*D* plot showing the corresponding counts for each sample at the various *Bragg* angles (θ). Figure 1b is a 2-*D* plot where the facets can be analyzed. The XRD analysis of the *in-house* IrO_2 electrocatalysts synthesized at 350 °C reveals an amorphous phase known to consist of smaller particle sizes. The (101) facet (at *Bragg* angle ~35°) was the main diffraction peak for samples synthesized at 350 °C. The (101) is a preferential facet of IrO_2 and is a close-packed plane for the Ir atom [21]. The *in-house* IrO_2 electrocatalyst synthesized at 400 °C, IH_IrO_2_400 °C_1:10, shows a rutile type oxide phase and shows an increase in crystallinity evident by sharper diffraction peaks and was accompanied by an increase in the particle size. At higher temperatures, crystallization and sintering occur. Toshinaga et al. [22] also observed increasing crystallinity with increasing synthesis temperature.

The average crystallite sizes for all samples were calculated from the (101) facet using the *Scherrer* formula:

$$d = 0.9\lambda / \beta \cos \theta \quad (3)$$

where d = average crystallite/particle size, 0.9 = shape factor, λ = wavelength of X-ray, β = peak width at half peak height in radians, θ = *Bragg* angle. Calculated average sizes are tabulated in Table 1.

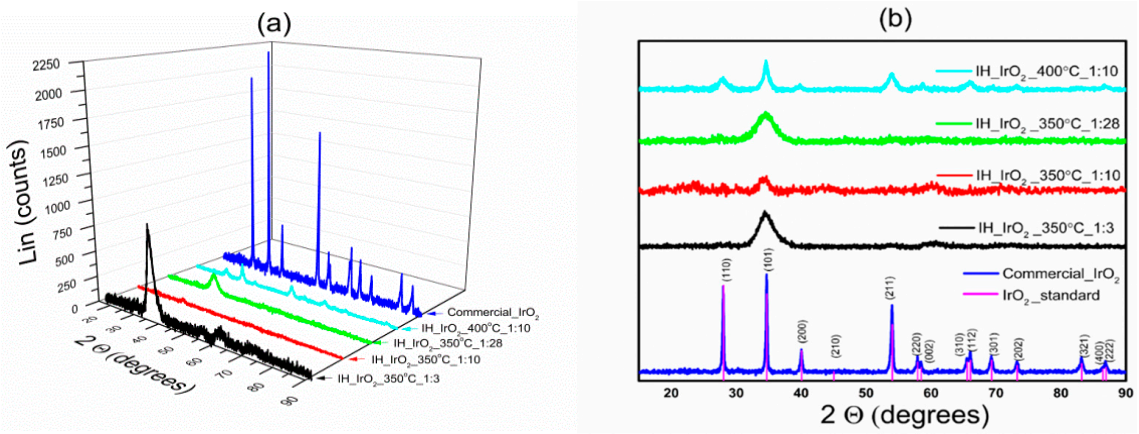

Figure 1. (**a**) 3-D plot of X-ray diffraction (XRD) patterns for *in-house* IrO_2 and commercial IrO_2. (**b**) 2-D plot of XRD patterns for *in-house* IrO_2 and commercial IrO_2.

Table 1. Average particle/crystallite sizes for the *in-house* and commercial IrO_2 samples.

Sample Name	Average Particle Size (nm) by *Scherrer* Formula	Average Particle Size (nm) by TEM
IH_IrO_2_350 °C_1:3	3.4	2.6 ± 0.6
IH_IrO_2_350 °C_1:10	4.2	2.2 ± 0.4
IH_IrO_2_350 °C_1:28	2.9	2.5 ± 0.5
IH_IrO_2_400 °C_1:10	13.9	9.7 ± 11.5
Commercial_IrO_2	41.1	216.1 ± 152.46

An increase in particle size is associated with a decrease in electrochemical surface area (ECSA) of the electrocatalysts [15,23]. Electrocatalysts should have a microstructure that maximizes the ECSA [24]. The (110) facet, another preferential facet of IrO_2, became more noticeable as crystallinity increased with the increase in temperature. The commercial IrO_2 sample was highly crystalline with a significant increase in the particle size. This suggests that the synthesis or the calcining temperature was significantly higher than the temperatures used for the *in-house* samples. No metallic Ir was observed.

Figure 2 shows the TEM images of the *in-house* IrO_2 and commercial IrO_2 electrocatalysts. TEM images for *in-house* IrO_2 synthesized at 350 °C shows particle sizes less than 5 nm while the *in-house* IrO_2 sample synthesized at 400 °C shows an increase in crystallinity and average particle size to about 10 nm. The measured average particle sizes are tabulated in Table 1. From the inset bar graph in Figure 2d it can be seen that sample IH_IrO_2_400 °C_1:10 exhibits a significant percentage of small particles less than 10 nm and to a much lesser extent exhibits larger needle shaped crystallites/particles. Smaller particle sizes are desirable as it effectively increases the number of surface atoms with respect to the bulk thereby increasing the OER activity per gram of catalyst [25].

The results for average particle size obtained by TEM for the *in-house* electrocatalysts are consistent with the XRD results. However, the TEM images for the commercial IrO_2 electrocatalyst show much larger rod-like structures of a few hundred nanometers in length, much larger than estimated using the *Scherrer* formula. Figure 3a,b shows the TGA and DTA plots for the *in-house* and commercial IrO_2 electrocatalysts respectively. From Figure 3a, the weight loss observed up to 100 °C is associated with the removal of physisorbed water molecules. The steady weight loss between 200 and 800 °C is due to the removal of chemisorbed water molecules (water of crystallization). The higher water loss for the samples synthesized at 350 °C is typical of amorphous IrO_2 while the low weight loss due to chemisorbed water for the sample synthesized at 400 °C and the commercial IrO_2, is typical of crystalline IrO_2. Furthermore, Hackwood et al. [26] have also shown that during this temperature range there is a phase transition from amorphous to crystalline represented by an exothermic peak. At 800 °C there is a major weight due to degradation of IrO_2 to IrO which corresponds to an endothermic peak as observed in Figure 3b [27,28]. The endothermic peak observed at about 220 °C for all samples are due to the removal of the chemisorbed water molecules. There is an additional endothermic peak occurring

at about 410 °C and 440 °C for samples IH_IrO_2_350 °C_1:3 and IH_IrO_2_350 °C_1:10 respectively. These two peaks may also be due to the removal of chemisorbed water molecules indicating that the samples synthesized at 350 °C are more hydrated IrO_2. The conversion of any unreacted Ir precursor is unlikely as the analyses were performed under argon flow. Table 2 summarizes the weight losses for each sample at three at temperatures intervals, i.e., 100 °C, 750 °C and ~1000 °C.

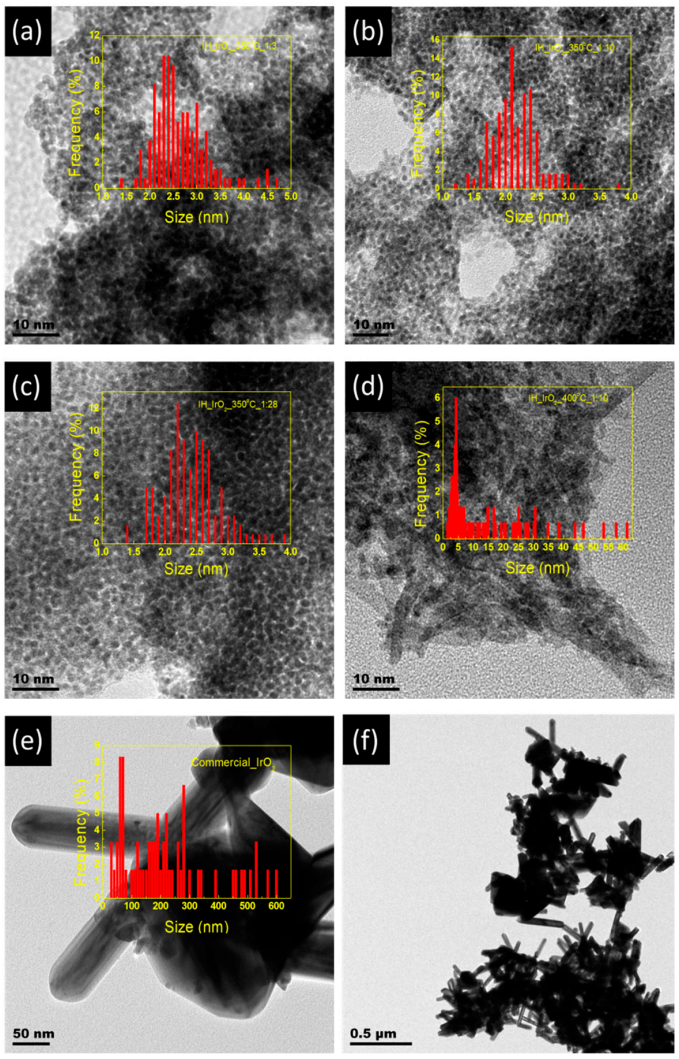

Figure 2. Transmission electron microscope (TEM) images of (**a**) IH_IrO_2_350 °C_1:3, (**b**) IH_IrO_2_350 °C_1:10, (**c**) IH_IrO_2_350 °C_1:28, (**d**) IH_IrO_2_400 °C_1:10, (**e**,**f**) Commercial_IrO_2.

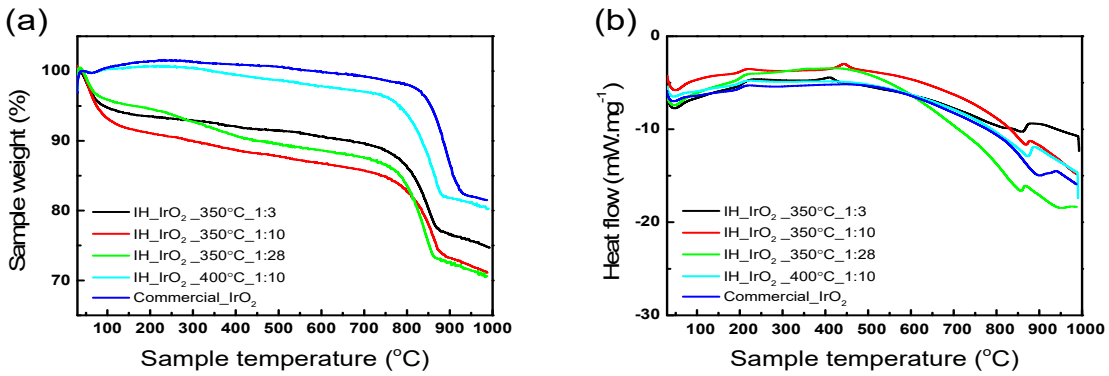

Figure 3. (**a**) Thermal gravimetric analysis (TGA) and (**b**) Differential thermal analysis (DTA) of *in-house* and commercial_IrO_2.

Table 2. Percentage weight loss during thermal gravimetric analysis (TGA).

Sample Name	% Weight Loss at 100 °C	% Weight Loss at 750 °C	% Weight Loss at ~1000 °C
IH_IrO_2_350 °C_1:3	5.3	11.3	25.3
IH_IrO_2_350 °C_1:10	6.8	15.1	29.1
IH_IrO_2_350 °C_1:28	4.2	13.4	29.6
IH_IrO_2_400 °C_1:10	N/A	3.8	19.6
Commercial_IrO_2	N/A	1.4	18.6

EDS analyses were performed to determine the elemental composition of the *in-house* IrO_2 samples. The sample synthesized at 400 °C displays the highest Ir content lending support that the samples synthesized at 350 °C are a more hydrated form of IrO_2. Table 3 summarizes the elemental compositions for the four *in-house* IrO_2 samples. Only in sample IH_IrO_2_350 °C_1:28 was a very low amount of chloride detected. It should be mentioned that very small peaks corresponding to Cl was also observed for the other samples however the areas under these peaks were too small for the instrument to assign any value to these peaks indicating that these were trace amounts. All samples synthesized at 350 °C showed the presence of about 2 weight percent Na while the sample synthesized at 400 °C had less than 1 weight percent Na present. These results suggest that at the lower temperature of 350 °C more of the $NaNO_3$ reagent may have remained unreacted and was not removed during the filtration step.

Table 3. Energy dispersive spectroscopy (EDS) analysis for the elemental composition of the *in-house* IrO_2 electrocatalysts.

Element	IH_IrO_2_350 °C_1:3		IH_IrO_2_350 °C _1:10		IH_IrO_2_350 °C_1:28		IH_IrO_2_400 °C_1:28	
	Weight %	Atomic %	Weight %	Atomic %	Weight %	Atomic %	Weight %	Atomic %
O	16.13	63.69	14.68	66	14.71	62.2	14.82	66.29
Ir	81.34	29.58	82.89	27.39	81.86	28.82	84.45	31.35
Na	2.35	6.73	2.25	6.61	2.35	6.91	0.73	2.26
Cl	-	-	-	-	1.09	2.07	-	-

2.2. Electrochemical Characterization

2.2.1. The Effect of the $H_2IrCl_6 \cdot xH_2O$ to $NaNO_3$ Mass Ratio

The mass of the $H_2IrCl_6 \cdot xH_2O$ precursor was held constant while the mass of the $NaNO_3$ was varied. In our previous paper [29], excess $NaNO_3$ up to 28 times the mass of the $H_2IrCl_6 \cdot xH_2O$ precursor was used during the fusion reaction to ensure that complete reaction took place and did not became the limiting factor. The original method by Adams et al. [19] used a 1:10 ratio while another study by Liu et al. [30] also investigated a 1:10 ratio as their lower limit. However, when considering upscaling a method, it becomes important to simplify the process to ensure that minimum cost is involved, and waste is carefully controlled. Large volumes require larger reactors, significantly adding to production costs. Furthermore, handling of high volumes of oxidizing materials becomes a significant safety hazard. Another key point for reducing the amount of $NaNO_3$ is to facilitate the reduction of pure water requirement during the filtration process as well as waste reduction. In this study, three mass ratios (1:3, 1:10 and 1:28) of $H_2IrCl_6 \cdot xH_2O$ to $NaNO_3$ were investigated. Figure 4 shows the electrochemical analyses of the IrO_2 samples synthesized using the various $H_2IrCl_6 \cdot xH_2O$ to $NaNO_3$ mass ratios as well as the commercial IrO_2. The synthesis temperature used was 350 °C.

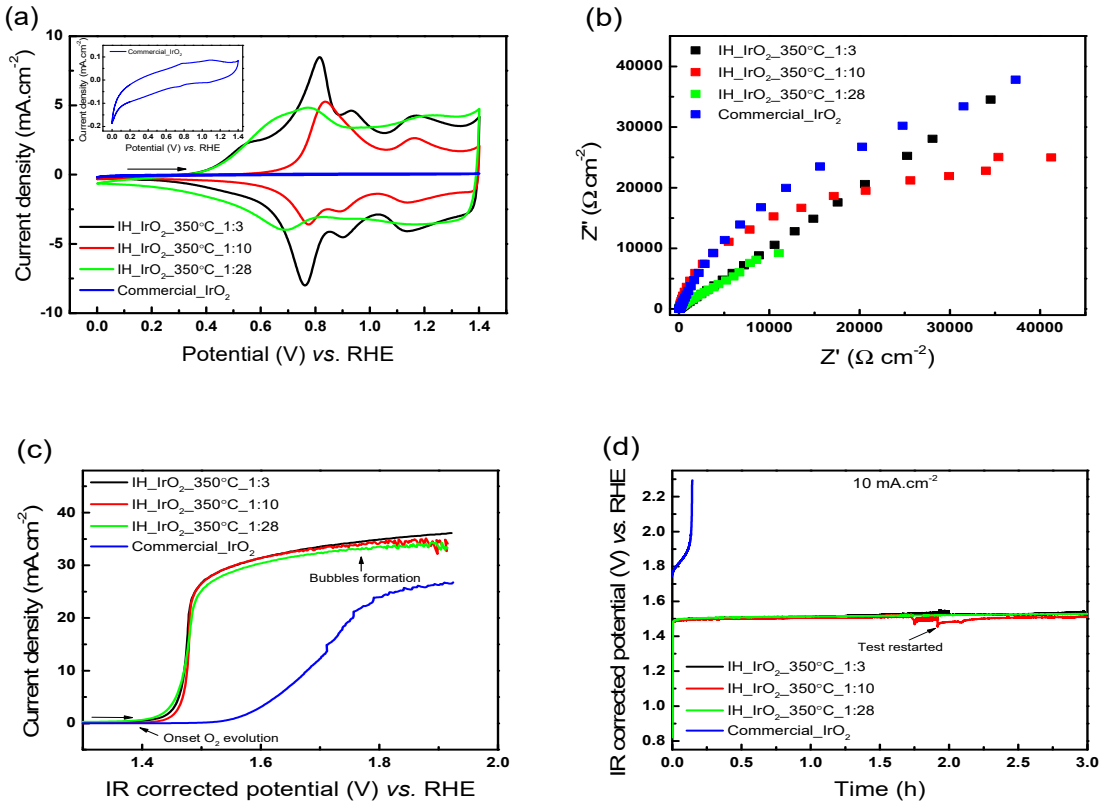

Figure 4. Electrochemical analyses of the *in-house* IrO_2 synthesized using various $H_2IrCl_6{\cdot}xH_2O$ to $NaNO_3$ ratios and commercial IrO_2 (**a**) Cyclic voltammetry (CV) analysis at 20 $mV{\cdot}s^{-1}$ potential scan rate, (**b**) Electrochemical impedance (EIS) analysis, (**c**) Linear sweep voltammetry (LSV) analysis at 2 $mV{\cdot}s^{-1}$ and (**d**) Chronopotentiometry (CP) analysis at 10 $mA{\cdot}cm^{-2}$.

Figure 4a shows the CVs where the potential was cycled between 0 V and +1.4 V vs. reversible hydrogen electrode (RHE) at a potential scan rate of 20 $mV{\cdot}s^{-1}$ in 0.5 M H_2SO_4. The shape of the voltammetric curves for the three *in-house* samples appears to be influenced by the amount of $NaNO_3$ used during the fusion reaction with the potentials for the redox couples shifting slightly. Samples IH_IrO_2_350 °C_1:3, IH_IrO_2_350 °C_1:10 and IH_IrO_2_350 °C_1:28 shows two redox couples, i.e., Ir(III)/Ir(IV) and Ir(IV)/Ir(V), with the Ir(III) → Ir(IV) oxidation peak reaching a maximum current density at +0.82 V, +0.83 V and +0.77 V vs. RHE for IH_IrO_2_350 °C_1:3, IH_IrO_2_350 °C_1:10 and IH_IrO_2_350 °C_1:28 respectively. In the case of Ir(IV) → Ir(V), the oxidation peaks reached maximum current densities at +1.17 V, +1.15 V and +1.23 V vs. RHE for IH_IrO_2_350 °C_1:3, IH_IrO_2_350 °C_1:10 and IH_IrO_2_350 °C_1:28 respectively. The CVs for samples IH_IrO_2_350 °C_1:3 and IH_IrO_2_350 °C_1:10 have shapes similar to those reported for hydrous iridium oxide films. The Ir(IV)/Ir(V) redox peak has significantly less charge associated with it which can be interpreted as a partial oxidation limited by repulsion from neighbouring Ir(VI) sites. These samples also display additional peaks at about 0.9 V for both forward and reverse scans which appears to separate from the Ir(III)/Ir(IV) couple. It is unclear to the true origin of these peaks but it may be due to interactions within the layer, distribution of formal potentials, coupled ion-electron transfer or a change in the mass transport in the layer as the potential is varied [31]. The oxidation/reduction of an impurity in the layer, such as the Na detected by EDS, may be ruled out as this additional peak is not noticed for samples IH_IrO_2_350 °C_1:28 and IH_IrO_2_400 °C_1:10. These peaks are most likely due to the presence of Ir(III) active sites with different formal potentials, oxidizing/reducing at slightly shifted potentials. Furthermore, due to incomplete decomposition, the presence of the Ir precursor in an oxide phase having an oxyhydroxide species may have the ability to act as active sites [23]. The mechanism for the Ir(III)/Ir(IV) redox transition is suggested to take place through the double ion-electronic

injection (or ejection) of electron and counter ion (H^+ or OH^-), compensating for the change of charge on the oxide. This mechanism requires the formation of an hydrated oxide on the surface [23]. During this redox transition, Ir(III)-OH_2 is oxidized to two Ir(IV)-OH. For the second redox transition an oxo-hydroxo Ir(IV)/Ir(V) or dioxo Ir(IV)/Ir(V) intermediate could be formed. However, ensemble effects are expected to suppress the possibility of two adjacent Ir(V)=O moieties thus only part of the surface hydroxyl groups are oxidized. This second redox step commonly overlaps with the OER [31]. In the potential window scanned, i.e., 0 V to +1.4 V vs. RHE, samples IH_IrO_2_350 °C_1:3 and IH_IrO_2_350 °C_1:28 also displays a higher negative current upon reaching 0 V vs. RHE on the reverse scan (cathodic). This usually indicates that some species that were oxidized with the anodic scan did not completely reduce during the cathodic scan hence the non-zero current meaning that the reaction is not fully reversible. The commercial IrO_2 show very low current density thus cannot be properly displayed in this graph but was added as an inset graph. The commercial IrO_2 catalyst also shows the two redox couples Ir(III)/Ir(IV) and Ir(IV)/Ir(V). Commercial_IrO_2 displays a strong negative tail at about 0 V vs. RHE upon the cathodic potential scan attributed to hydrogen adsorption (H_{ads}).

Figure 4b shows the EIS analysis as a *Nyquist* plot which was obtained by perturbing the system from 100,000 Hz to 0.1 Hz at an amplitude of 5 mV. The high frequency region of the *Nyquist* plot is associated with the resistance of the electrolyte and the physical properties of the electrode and can thus be used to perform ohmic drop compensation. No significant differences were noticed at the high frequency real impedance intercept (Z') indicating that the electrolyte and the electrode electronic conductivity were very similar. There are some differences in the charge transfer resistances region of the *Nyquist* plots. Parameters that could impact the impedance in this region is the Nafion® ionomer content in the catalyst layer covering active catalyst sites [32] as well as the porosity of the electrodes. No mass transfer resistance is shown as the electrolyte is sufficiently conductive.

Figure 4c shows the polarization curves obtained using the LSV technique. The potential was scanned from +1.3 V to +2 V vs. RHE at a potential scan rate of 2 $mV \cdot s^{-1}$ and 1600 rpm rotating disc electrode (RDE) speed. The potential was corrected using the EIS results obtained at high frequencies. The onset of the OER starts at about +1.4 V vs. RHE for the three *in-house* samples and at about +1.52 V vs. RHE for the commercial sample. At higher potentials above 1.7 V vs. RHE, significant bubble formation was observed for samples IH_IrO_2_350 °C_1:10 and IH_IrO_2_350 °C_1:28. The *in-house* IrO_2 samples showed significantly better performance than the commercial IrO_2 sample. The large particle sizes of the commercial catalyst as observed through XRD and TEM would result in a much lower ECSA hence a lower performance of the commercial IrO_2 sample. Moreover, the samples IH_IrO_2_350 °C_1:3 and IH_IrO_2_350 °C_1:10 displayed the highest current densities over the potential window of +1.5 V to +1.8 V vs. RHE.

Figure 4d shows the CP results obtained at 10 $mA \cdot cm^{-2}$ for 3 h at a RDE speed of 1200 rpm. Commercial_IrO_2 was very unstable under these test conditions and reached high potentials within a few minutes. The *in-house* IrO_2 electrocatalysts were very stable over the 3 h duration. Significant bubble formation caused the experiment to be stopped for sample IH_IrO_2_350 °C_1:10 to remove the bubble that covered the entire surface of the electrode. The same result was obtained with repeated tests for this sample. After the restart the potential remained slightly lower than before the bubble covered the electrode surface. The reason for the lower potential after restart is not clear. However, the three *in-house* IrO_2 samples showed very similar activity and stability during the 3hour test duration thus indicating that the excess $NaNO_3$ is not necessary and only adds to the cost of the synthesis method.

2.2.2. Effect of Synthesis Temperature

In our previous paper [29], the effect of the synthesis temperature on the electrochemical performance of the IrO_2 electrocatalysts synthesized using a modified Adams method, were investigated. The results showed that as the synthesis temperature was increased the IrO_2 electrocatalyst became more crystalline resulting in larger particle sizes and reduced electrochemical performance. Here, we only compare two temperatures, i.e., 350 °C and 400 °C to confirm our previous findings. Figure 1; Figure 2 confirmed that the

increase in synthesis temperature resulted in a more crystalline structure with larger particle sizes. Figure 5 shows results obtained from electrochemical analyses when comparing samples IH_IrO_2_350 °C_1:10 and IH_IrO_2_400 °C_1:10.

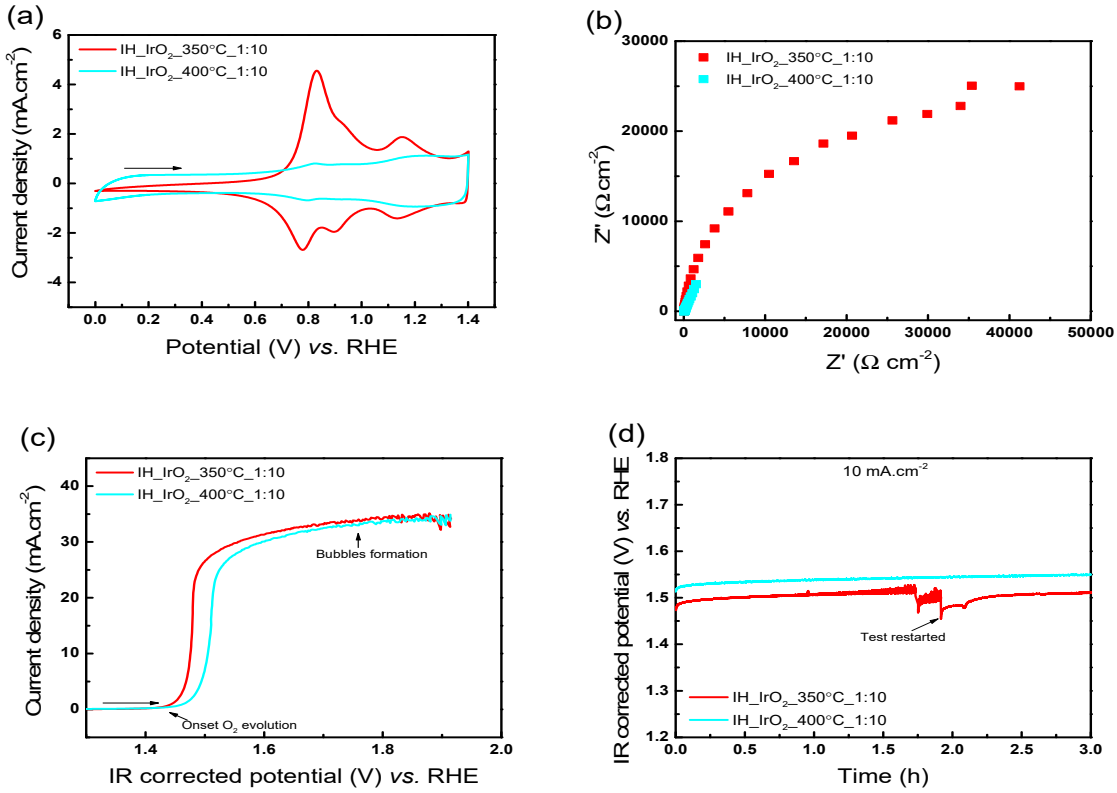

Figure 5. Electrochemical analyses of IH_IrO_2_350 °C_1:10 and IH_IrO_2_400 °C_1:10 (**a**) CV analysis at 20 mV·s^{-1} potential scan rate, (**b**) EIS analysis, (**c**) LSV analysis at 2 mV·s^{-1} and (**d**) CP analysis at 10 mA·cm^{-2}.

Figure 5a shows the CVs for IH_IrO_2_350 °C_1:10 and IH_IrO_2_400 °C_1:10. Sample IH_IrO_2_400 °C_1:10 shows the two redox couples, i.e., Ir(III)/Ir(IV) and Ir(IV)/Ir(V) reaching maximum anodic peak current density at +0.83 V and +1.23 V vs. RHE respectively. The CV curve for IH_IrO_2_400 °C_1:10 is typical of the IrO_2 synthesized at higher temperatures. A much lower current density was measured compared to sample IH_IrO_2_350 °C_1:10. Non-faradaic current due to double-layer charging is visible for sample IH_IrO_2_400 °C_1:10 between 0 V and +0.7 V vs. RHE. At 0 V vs. RHE, there is an onset of a cathodic negative tail of capacitive behaviour [23]. The capacitive behaviour of IrO_2 comes from the pseudo-capacitance (due to proton exchange) and the double layer capacitance (due to ion adsorption) [20].

Figure 5b shows the EIS analysis as a *Nyquist* plot which was obtained between 100,000 Hz and 0.1 Hz at 5 mV amplitude. A low charge transfer resistance (compared to samples synthesized at 350 °C) is observed for IH_IrO_2_400 °C_1:10 while no mass transfer resistance is observed. Figure 4c,d shows the polarization curves and chronopotentiometry results for the two samples respectively. In both tests the IrO_2 electrocatalyst synthesized at lower temperature, i.e., 350 °C, displays better activity although both samples appear to be stable over the 3 h duration of the CP test. During the LSV polarization curve measurement, the onset of the OER takes place at a slightly more positive potential for IH_IrO_2_400 °C_1:10.

2.2.3. Determination of Electrochemical Surface Areas Estimates

Electrochemical surface areas (ECSA) were determined from the voltammetric charge obtained through integration of the anodic portion of CVs between +0.4 V and +1.4 V vs. RHE. CVs were

obtained at various scan rates from 0.005 V to 0.5 V. The oxidation states of IrO_2 is dependent on the electrode potential and the pseudocapacitive behaviour of the electrode is a result of solid state redox transitions due to the transfer of hydrated protons at the oxide/solution interface [33]. The pseudocapacitive process can be can be illustrated by Equation (4).

$$MO_x(OH)_y + \delta H^+ + \delta e^- \leftrightharpoons MO_{x-\delta}(OH)_y + \delta \quad (4)$$

where M is the metal center of the active site and δH^+ is the amount of protons exchanged with the solution. If each portion of the active surface oxidized or reduced is considered as an active surface site then the pseudocapacitive charge density (Q_a*) can be considered as an indirect measurement of the ECSA. The oxide layer typically consists of a microstructure that includes narrow pores, cracks, etc. and these regions are referred to as the internal surface area. At slow potential scan rates, this internal surface area become accessible to voltammetric response however as the potential scan rate increases, this internal surface area becomes progressively excluded from the voltammetric response. It is assumed that the total voltammetric charge density (Q_t*) is the result of two contributions:

$$Q_t^* = Q_i^* + Q_e^* \quad (5)$$

where Q_i* and Q_e* are the internal and external voltammetric charge densities respectively. A linear plot of Q_a* versus $1/\sqrt{v}$ can be used to determine Q_e* by extrapolating the scan rate to infinity. The total voltammetric charge density (Q_t*) can be determined by plotting $1/Q_a$* versus the $\sqrt{v}$ and extrapolating the potential scan rate to zero. The internal voltammetric charge density can then be obtained by Equation (6).

$$Q_i^* = Q_t^* - Q_e^* \quad (6)$$

The electrochemical porosity (Φ) can also be determined from the ratio between the internal and total voltammetric charge densities as illustrated by Equation (7).

$$\Phi = \frac{Q_i^*}{Q_t^*} \quad (7)$$

High values of Φ indicates that a significant portion of the active sites are located in the deepest regions of the surface defects (narrow pores, cracks, etc.) [33,34]. Figure 6a–d shows plots used for estimating the total voltammetric charge (Q_t*) and external voltammetric charge (Q_e*). Figure 6a shows the the dependence of the anodic charge density (Q_a*) on the scan rate. As the potential scan rate increases, Q_a* decreases as proposed above. For sample IH_IrO_2_400 °C_1:10, the plot shows that the Q_a* only decreases minimally with increasing potential scan rate. This suggests that either both internal and external active sites are accessible over all potential scan rates or that the internal active sites are inaccessible even at very slow scan rates. This may be influenced by the catalyst layer morphology and thickness which may hinder or promote proton diffusion into the layer.

Figure 6b shows the Q_a*/Q_c* ratio as the potential scan rate is varied. At slow potential scan rates (<0.2 $V \cdot s^{-1}$), the samples show good reversibility. From Figure 6c, the Q_e* can be determined which can be related to the ECSA. At high potential scan rates, there is a significant decrease in the Q_a* observed for the electrocatalysts synthesized at 350 °C due to irreversibility and uncompensated ohmic drops which may lead to errors when extrapolating the Q_e* [34]. These points have been excluded to minimize errors. Figure 6d shows the plots used to estimate Q_t*. A summary of the estimated results are found in Table 4. Samples IH_IrO_2_350 °C_1:3 and IH_IrO_2_350 °C_1:28 shows the highest estimates of Q_e* however it appears that this method for ECSA calculation may not be suitable for sample IH_IrO_2_400 °C_1:10 since the method strongly relies on the dependence of Q_a* with varying potential scan rates.

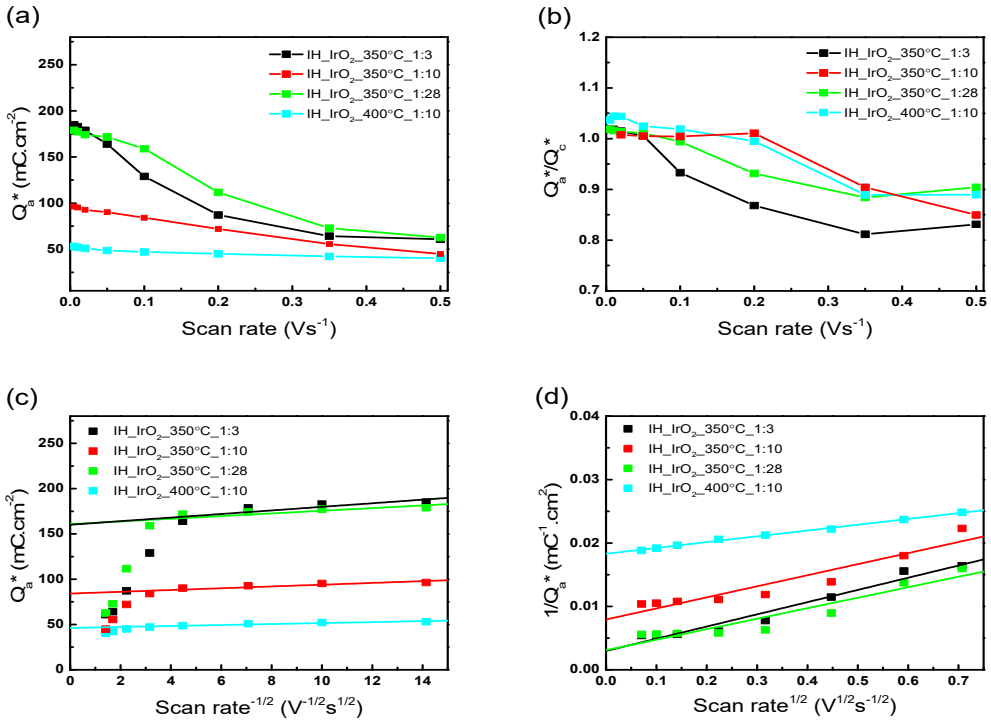

Figure 6. Estimation of electrochemical surface area (ECSA) for *in-house* IrO_2 electrocatalysts (**a**) Dependence of Q_a* on the potential scan rate. (**b**) Influence of the potential scan rate on the Q_a*/Q_c* ratio. (**c**) Extrapolation of Q_a* as the potential scan rate $\rightarrow \infty$. (**d**) Extrapolation of Q_a* as the potential scan rate $\rightarrow 0$.

Table 4. Extrapolated results for estimated ECSA and electrochemical porosity.

Sample Name	Q_t* (mC·cm^{-2})	Q_e* (mC·cm^{-2})	Q_i* (mC·cm^{-2})	Φ
IH_IrO_2_350 °C_1:3	339.8	160.1	179.7	0.53
IH_IrO_2_350 °C_1:10	127.4	84.2	43.2	0.34
IH_IrO_2_350 °C_1:28	323.8	160.9	162.9	0.50
IH_IrO_2_400 °C_1:10	54.6	46.2	8.4	0.15

2.2.4. Durability Studies of In-House IrO_2 Samples

It has been suggested that amorphous (hydrated) IrO_2 is more active towards the OER compared to the more crystalline (anhydrous) IrO_2 electrocatalyst but suffers from severe corrosion whereas the crystalline IrO_2 electrocatalyst are more stable [35]. Therefore, CV was used as a tool to measure the durability of the in-house IrO_2 samples. CV experiments were performed between 0 V and +1.4 V vs. RHE at a potential scan rate of 20 mV·s^{-1} at an initial start, after 1200 CV cycles and after 3000 cycles. CV cycles were performed between +0.2 V and +1.4 V vs. RHE at a potential scan rate of 200 mV·s^{-1} while no RDE rpm was used. Figure 7 shows the CV plots for the *in-house* IrO_2 electrocatalysts with inset graphs showing the change in charge (charge vs. time plot) over the 3000 cycles. From the CV durability measurements, sample IH_IrO_2_350 °C_1:3 shows the least decrease in anodic charge density after the 3000 cycles suggesting that the sample is the more stable of the *in-house* IrO_2 electrocatalysts over the duration of the study. However, IH_IrO_2_400 °C_1:10 also shows good stability with a 6% decrease in anodic charge density and shows virtually no decrease in anodic charge density after the 1200 cycles which may suggest that with increased cycling duration it may be the most stable of the in-house IrO_2 electrocatalysts.

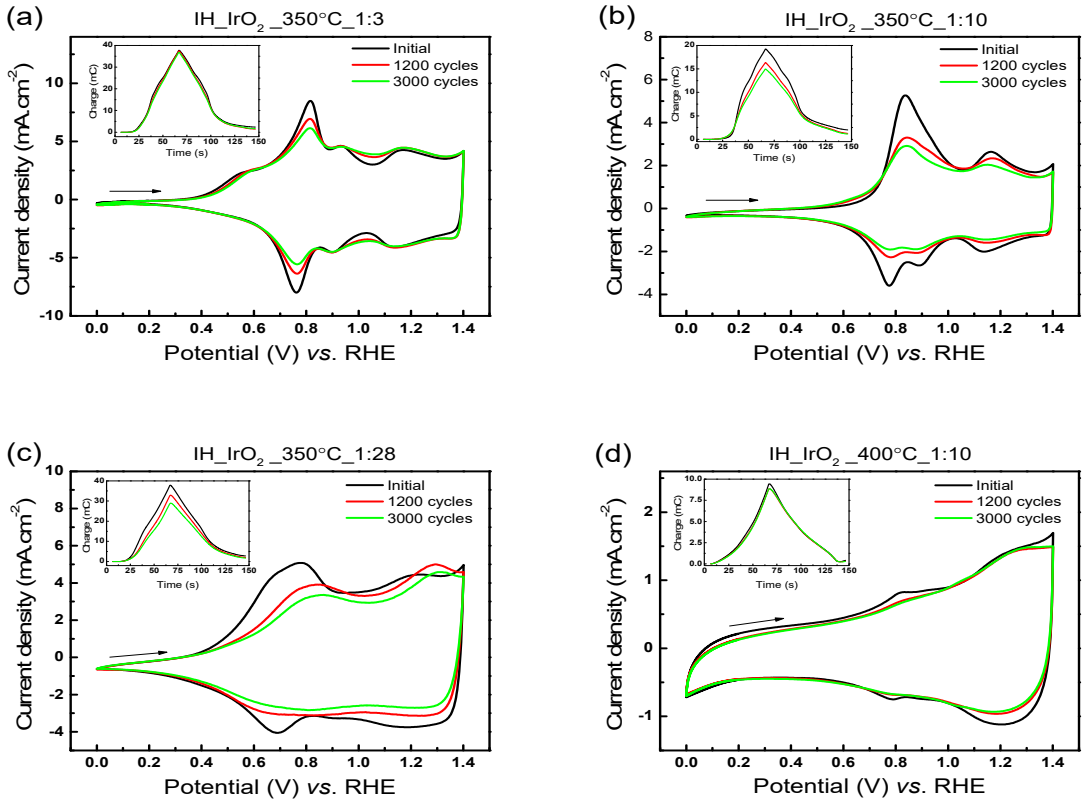

Figure 7. Durability CV analyses of the *in-house* IrO_2 samples at 20 $mV \cdot s^{-1}$ potential scan rate. (**a**) IH_IrO_2_350 °C_1:3, (**b**) IH_IrO_2_350 °C_1:10, (**c**) IH_IrO_2_350 °C_1:28 and (**d**) IH_IrO_2_400 °C_1:10. Insets are the charge vs. time plots.

Table 5 summarizes the change in the anodic charge density (Q_a*) for the four samples. The percentage in brackets represents the decrease in Q_a* from the initial value.

Table 5. Anodic charge density measured during durability study.

Sample Name	Q_a* ($mC \cdot cm^{-2}$) Initial	Q_a* ($mC \cdot cm^{-2}$) after 1200 Cycles	Q_a* ($mC \cdot cm^{-2}$) after 3000 Cycles
IH_IrO_2_350 °C_1:3	192.4	191.1 (−0.7%)	187.6 (−1.6%)
IH_IrO_2_350 °C_1:10	98.1	83.3 (−15.1%)	76.3 (−22.2%)
IH_IrO_2_350 °C_1:28	192.8	167.5 (−13.1%)	147.4 (−23.5%)
IH_IrO_2_400 °C_1:10	48.1	45.2 (−6.0%)	45.2 (−6.0%)

The two samples synthesized with the 1:10 $H_2IrCl_2 \cdot xH_2O$ to $NaNO_3$ mass ratio, i.e., IH_IrO_2_350 °C_350 and IH_IrO_2_400 °C_1:10, showed much lower anodic charge densities. Figure 8 shows the polarization curves measured before CV cycling, after 1200 CV cycles and after 3000 CV cycles. The insets show the EIS measured before CV cycling, after 1200 CV cycles and after 3000 CV cycles.

Sample IH_IrO_2_400 °C_1:10 shows a slight decrease in current density from the initial measurement while the other samples remained stable. Table 6 summarizes the anodic current density (J_a) for the four samples at +1.6 V vs. RHE over the duration of the durability study.

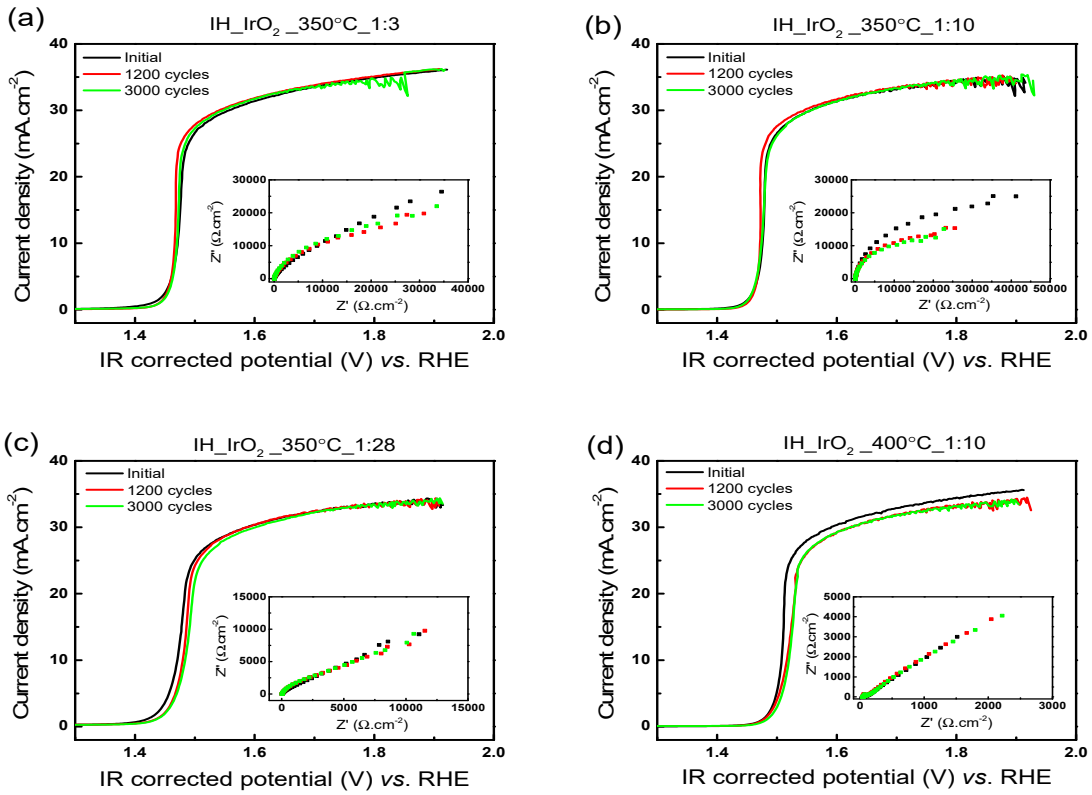

Figure 8. LSV analyses at 2 $mV \cdot s^{-1}$ potential scan rate of the *in-house* IrO_2 electrocatalysts during the durability experiment. (**a**) IH_IrO_2_350 °C_1:3, (**b**) IH_IrO_2_350 °C_1:10, (**c**) IH_IrO_2_350 °C_1:28 and (**d**) IH_IrO_2_400 °C_1:10. Insets are of EIS analysis over durability experiment.

Table 6. Anodic current density measured at 1.6 V vs. RHE during the durability study.

Sample Name	J_a ($mA \cdot cm^{-2}$) Initial	J_a ($mA \cdot cm^{-2}$) after 1200 Cycles	J_a ($mA \cdot cm^{-2}$) after 3000 Cycles
IH_IrO_2_350 °C_1:3	31.4	31.8	31.7
IH_IrO_2_350 °C_1:10	31.3	31.7	31.3
IH_IrO_2_350 °C_1:28	30.4	30.4	30.0
IH_IrO_2_400 °C_1:10	30.3	29.3	29.3

Sample IH_IrO_2_350 °C_1:28 shows a slight increase to a more positive OER onset potential as can also be observed from the CV plot in Figure 4c. Although there was some noticeable decrease in the Q_a* observed from the CV durability plots these did not relate to a significant impact on the polarization curves for the three samples synthesized at 350 °C. It may be that the decrease in Q_a* was related to a reduction in charge contribution through non-faradaic processes such as capacitance and double-layer charging. Furthermore, the OER occurs at potentials anodic of the Ir(IV)/Ir(V) redox couple [36]. The lower ECSA estimated for samples IH_IrO_2_350 °C_1:10_ and IH_IrO_2_400 °C_1:10 also did not have a negative impact on the OER performances of these samples. Hu et. al. also found that the ECSA estimated from the Q_a*, which is obtained in the oxygen evolution double layer region, may not be most suitable method for determining true ESCA. They suggested the charge likely only revealed the active area in the measured potential window while the OER occurs at higher potentials [37].

3. Materials and Methods

3.1. Electrocatalyst Synthesis

$H_2IrCl_6 \cdot xH_2O$ (Alfa Aesar, Haverhill, MA, USA) was used as precursor to synthesize the IrO_2 electrocatalysts. An amount of 0.36 g $H_2IrCl_6 \cdot xH_2O$ was dissolved in 10 mL isopropanol (IPA,

Sigma, St. Louis, MO, USA) and magnetically stirred for 30 min. Finely ground $NaNO_3$ (Alfa Aesar, Havervill. MA, USA) was added to the solution, which was then further stirred for 30 min. Three mass ratios (1:3, 1:10 and 1:28) of $H_2IrCl_6 \cdot xH_2O$ to $NaNO_3$ were investigated with the mass of $H_2IrCl_6 \cdot xH_2O$ held constant. The mixture was then dried in an oven for 30 min at 110 °C. The dried catalyst precursor/$NaNO_3$ mixture was then reacted in a furnace for 120 min at 350 °C. The temperature was also increased to 400 °C to evaluate the effect of synthesis temperature on the electrocatalyst morphology and electrochemical performance. No additional calcining step was performed. The obtained metal oxide was cooled and filtered with 1.5 L of ultrapure water obtained using the Milli-Q® Direct 8 (MilliporeSigma, Burlington, MA, USA) to remove the unreacted $NaNO_3$. The final step was to dry the metal oxide in an oven for 120 min at 100 °C then cool down and air dry overnight. A commercial IrO_2 electrocatalyst (Sigma, St. Louis, MO, USA) was used for comparison purposes.

3.2. Preparation of the Working Electrode

A RDE (Pine Research Instrumentation, Inc., Durham, NC, USA) with 0.196 cm^2 working area was used for electrochemical experiments. The electrode was cleaned/polished using 0.05 μm deagglomerated alumina paste (Buehler, Lake Bluff, IL, USA) before and after each use followed by ultrasonication in ultrapure water for 15 min. The electrode was dried for 15 min at 2500 rotations per minute (rpm) at ambient conditions. The catalyst ink was prepared by combining 8 mg of the IrO_2 electrocatalyst, 50 μL 5 wt % Nafion® solution (Alfa Aesar, Havervill, MA, USA) and 1950 μL ultrapure water and ultrasonicating for 20 min. A micropipette was used to drop 30 μL of the catalyst ink onto the RDE. The working electrode was covered and dried overnight at ambient conditions. A catalyst loading of 0.45 mg cm^2 was obtained.

3.3. Physical Characterization

Physical phases and structures of the electrocatalysts were characterized by X-ray diffraction (XRD) employing the Bruker AXS D8 Advance diffractometer (Bruker, Billerica, MA, USA) using Cu K_α radiation (λ = 1.5406 Å) operating at 40 kV and 40 mA. The IrO_2 standard (K & K Laboratories Incorporated, Carlsbad, San Diego County, USA) used for peak allocation was synthesized at 900 °C for 6 h. Transmission electron micrographs were obtained using a FEI/Tecnai T20 (FEI Company, Hillsboro, OR, USA) operating at 200 kV. Thermal gravimetric analysis and differential thermal analysis were performed using the Perkin Elmer STA 8000 (Perkin Elmer, Inc., Waltham, MA, USA) between 30 °C and 1000 °C under 80 mL/min argon flow. EDS analysis was performed using the Carl Zeiss Auriga HR-SEM (Carl Zeiss AG, Oberkochen, Germany) with a 60 s collection time.

3.4. Electrochemical Characterization

Electrochemical analyses were performed at 25 °C and atmospheric pressure. Cell temperature was maintained using a circulating water bath (SMC). The RDE working electrode (as described in earlier), a 3 M Ag/AgCl reference electrode (Metrohm, Herisau, Switzerland), a Pt wire (1 cm^2 area) counter electrode and a 0.5 M H_2SO_4 electrolyte solution was used. All potentials in this work are reported versus the reversible hydrogen electrode (RHE). The Autolab potentiostat PGSTAT302N (Eco-Chemie/Metrohm, Ultrecht, Netherlands) was used for all electrochemical analyses. The electrolyte solution was purged with N_2 for 30 min before performing electrochemical measurements. The electrode was activated by CV cycling between 0 V and +1.2 V vs. RHE at a 200 $mV \cdot s^{-1}$ potential scan rate for 100 cycles.

4. Conclusions

IrO_2 electrocatalysts were synthesized using a modified Adams fusion method. The impact of the $NaNO_3$ to Ir precursor ratio on the electrocatalyst OER activity were investigated and it was found that excess $NaNO_3$ did not enhance the electrocatalyst OER activity. A higher synthesis temperature was shown to produce a more crystalline IrO_2 electrocatalyst with slightly lower OER

activity. Physical characterization analyses showed that the electrocatalysts synthesized at 350 °C were hydrous amorphous IrO_2 while the IrO_2 electrocatalyst synthesized at 400 °C became more anhydrous and crystalline. Electrochemical analyses have shown that all *in-house* IrO_2 showed good activity and stability towards the OER. However, analyses of the voltammetric charge did not show a direct correlation between the stability and activity under OER conditions. This lack in correlation may be due to the fact the OER occurs at higher potentials (potentials more anodic) than the potential window from where the voltammetric charges were calculated. This also seems to have affected the estimation of the ECSA for these electrocatalysts. Future research will explore determining the ECSA of these IrO_2 electrocatalysts using the mercury underpotential deposition technique. An anomalous redox peak, emanating from the Ir(III)/Ir(IV) redox couple, was observed for two of the IrO_2 electrocatalysts synthesized at 350 °C. Some suggestions were provided as to the origin of these peaks however further investigation is needed to determine the true origin of these peaks.

Author Contributions: C.F. performed the experiments, analyzed the data and wrote the article; B.J.B., B.G.P., V.L. and S.P. analyzed the data and wrote the article.

Funding: This research received no external funding.

Conflicts of Interest: The authors declare no conflict of interest.

References

1. Carmo, M.; Fritz, D.L.; Mergel, J.; Stolten, D. A comprehensive review on PEM water electrolysis. *Int. J. Hydrogen Energy* **2013**, *38*, 4901–4934. [CrossRef]
2. Cheng, Y.; Jiang, S.P. Advances in electrocatalysts for oxygen evolution reaction of water electrolysis—From metal oxides to carbon nanotubes. *Prog. Nat. Sci. Mater. Int.* **2015**, *25*, 545–553. [CrossRef]
3. Mohammadi, A.; Mehrpooya, M. A comprehensive review on coupling different types of electrolyzer to renewable energy sources. *Energy* **2018**, *158*, 632–655. [CrossRef]
4. Yu, H.; Danilovic, N.; Wang, Y.; Willis, W.; Poozhikunnath, A.; Bonville, L.; Capuano, C.; Ayers, K.; Maric, R. Nano-size IrOx catalyst of high activity and stability in PEM water electrolyzer with ultra-low iridium loading. *Appl. Catal. B* **2018**, *239*, 133–146. [CrossRef]
5. Cheng, J.; Zhang, H.; Ma, H.; Zhong, H.; Zou, Y. Study of carbon-supported IrO_2 and RuO_2 for use in the hydrogen evolution reaction in a solid polymer electrolyte electrolyzer. *Electrochim. Acta* **2010**, *55*, 1855–1861. [CrossRef]
6. Song, S.; Zhang, H.; Ma, X.; Shao, Z.; Baker, R.T.; Yi, B. Electrochemical investigation of electrocatalysts for the oxygen evolution reaction in PEM water electrolyzers. *Int. J. Hydrogen Energy* **2008**, *33*, 4955–4961. [CrossRef]
7. Marshall, A.T.; Sunde, S.; Tsypkin, M.; Tunold, R. Performance of a PEM water electrolysis cell using $Ir_xRu_yTa_zO_2$ electrocatalysts for the oxygen evolution electrode. *Int. J. Hydrogen Energy* **2007**, *32*, 2320–2324. [CrossRef]
8. Badam, R.; Hara, M.; Huang, H.-H.; Yoshimura, M. Synthesis and electrochemical analysis of novel IrO_2 nanoparticle catalysts supported on carbon nanotube for oxygen evolution reaction. *Int. J. Hydrogen Energy* **2018**, *43*, 18095–18104. [CrossRef]
9. Ma, Z.; Zhang, Y.; Liu, S.; Xu, W.; Wu, L.; Hsieh, Y.-C.; Liu, P.; Zhu, Y.; Sasaki, K.; Renner, J.N.; et al. Reaction mechanism for oxygen evolution on RuO_2, IrO_2, and RuO_2@IrO_2 core-shell nanocatalysts. *J. Electroanal. Chem.* **2018**, *819*, 296–305. [CrossRef]
10. Ahmed, J.; Mao, Y. Ultrafine Iridium Oxide Nanorods Synthesized by Molten Salt Method toward Electrocatalytic Oxygen and Hydrogen Evolution Reactions. *Electrochim. Acta* **2016**, *212*, 686–693. [CrossRef]
11. Chen, C.A.; Chen, Y.M.; Huang, Y.S.; Tsai, D.S.; Liao, P.C.; Tiong, K.K. Synthesis and structural characterization of twinned V-shaped IrO_2 nanowedges on TiO_2 nanorods via MOCVD. *J. Alloy Compd.* **2009**, *480*, 107–110. [CrossRef]
12. Siracusano, S.; Baglio, V.; Stassi, A.; Ornelas, R.; Antonucci, V.; Aricò, A.S. Investigation of IrO_2 electrocatalysts prepared by a sulfite-couplex route for the O_2 evolution reaction in solid polymer electrolyte water electrolyzers. *Int. J. Hydrogen Energy* **2011**, *36*, 7822–7831. [CrossRef]

13. Murakami, Y.; Ohkawauchi, H.; Ito, M.; Yahikozawa, K.; Takasu, Y. Preparations of ultrafine IrO_2-SnO_2 binary oxide particles by a sol-gel process. *Electrochim. Acta* **1994**, *39*, 2551–2554. [CrossRef]
14. Marshall, A.; Børresen, B.; Hagen, G.; Tsypkin, M.; Tunold, R. Electrochemical characterisation of $Ir_xSn_1-xO_2$ powders as oxygen evolution electrocatalysts. *Electrochim. Acta* **2006**, *51*, 3161–3167. [CrossRef]
15. Cheng, J.; Zhang, H.; Ma, H.; Zhong, H.; Zou, Y. Preparation of $Ir_{0.4}Ru_{0.6}Mo_xO_y$ for oxygen evolution by modified Adams' fusion method. *Int. J. Hydrogen Energy* **2009**, *34*, 6609–6613. [CrossRef]
16. Rasten, E.; Hagen, G.; Tunold, R. Electrocatalysis in water electrolysis with solid polymer electrolyte. *Electrochim. Acta* **2003**, *48*, 3945–3952. [CrossRef]
17. Shriner, R.L.; Adams, R. The preparation of palladous oxide and its use as a catalyst in the reduction of organic compounds, VI. *J. Am. Chem. Soc.* **1924**, *46*, 1683–1693. [CrossRef]
18. Zhang, Y.; Wang, C.; Mao, Z.; Wang, N. Preparation of nanometer-sized SnO_2 by the fusion method. *Mater. Lett.* **2007**, *61*, 1205–1209. [CrossRef]
19. Adams, R.; Shriner, R.L. Platinum oxides as a catalyst in the reduction of organic compounds. III, Preparation and properties of the oxide of platinum obtained by the fusion of chloroplatinic acid with sodium nitrate. *J. Am. Chem. Soc.* **1923**, *45*, 2171–2179. [CrossRef]
20. Puthiyapura, V.K.; Mamlouk, M.; Pasupathi, S.; Pollet, B.G.; Scott, K. Physical and electrochemical evaluation of ATO supported IrO_2 catalyst for proton exchange membrane water electrolyser. *J. Power Sources* **2014**, *269*, 451–460. [CrossRef]
21. Hu, J.M.; Meng, H.M.; Zhang, J.Q.; Cao, C.N. Degradation mechanism of long service life Ti/IrO_2–Ta_2O_5 oxide anodes in sulphuric acid. *Corros. Sci.* **2002**, *44*, 1655–1668. [CrossRef]
22. Yoshinaga, N.; Sugimoto, W.; Takasu, Y. Oxygen reduction behavior of rutile-type iridium oxide in sulfuric acid solution. *Electrochim. Acta* **2008**, *54*, 566–573. [CrossRef]
23. Grupioni, A.A.F.; Arashiro, E.; Lassali, T.A.F. Voltammetric characterization of an iridium oxide-based system: The pseudocapacitive nature of the $Ir_{0.3}Mn_{0.7}O_2$ electrode. *Electrochim. Acta* **2002**, *48*, 407–418. [CrossRef]
24. Lervik, I.A.; Tsypkin, M.; Owe, L.-E.; Sunde, S. Electronic structure vs. electrocatalytic activity of iridium oxide. *J. Electroanal. Chem.* **2010**, *645*, 135–142. [CrossRef]
25. Abbott, D.F.; Lebedev, D.; Waltar, K.; Povia, M.; Nachtegaal, M.; Fabbri, E.; Copéret, C.; Schmidt, T.J. Iridium Oxide for the Oxygen Evolution Reaction: Correlation between Particle Size, Morphology, and the Surface Hydroxo Layer from Operando XAS. *Chem. Mater.* **2016**, *28*, 6591–6604. [CrossRef]
26. Hackwood, S.; Dayem, A.H.; Beni, G. Amorphous-nonmetal-to-crystalline-metal transition in electrochromic iridium oxide films. *Phys. Rev. B* **1982**, *26*, 471–478. [CrossRef]
27. Kawar, R.K.; Chigare, P.S.; Patil, P.S. Substrate temperature dependent structural, optical and electrical properties of spray deposited iridium oxide thin films. *Appl. Surf. Sci.* **2003**, *206*, 90–101. [CrossRef]
28. Karimi, F.; Peppley, B.; Bazylak, A. Study of the Effect of Calcination Temperature on the Morphology and Activity of Iridium Oxide Electrocatalyst Supported on Antimony Tin Oxide (ATO) for PEM Electrolyser Technology. *ECS Trans.* **2015**, *69*, 87–98. [CrossRef]
29. Felix, C.; Maiyalagan, T.; Pasupathi, S.; Bladergroen, B.; Linkov, V. Synthesis and Optimisation of IrO_2 Electrocatalysts by Adams Fusion Method for Solid Polymer Electrolyte Electrolysers. *Micro Nanosyst.* **2012**, *4*, 186–191. [CrossRef]
30. Liu, Y.; Wang, C.; Lei, Y.; Liu, F.; Tian, B.; Wang, J. Investigation of high-performance IrO_2 electrocatalysts prepared by Adams method. *Int. J. Hydrogen Energy* **2018**, *43*, 19460–19467. [CrossRef]
31. Steegstra, P.; Busch, M.; Panas, I.; Ahlberg, E. Revisiting the Redox Properties of Hydrous Iridium Oxide Films in the Context of Oxygen Evolution. *J. Phys. Chem. C* **2013**, *117*, 20975–20981. [CrossRef]
32. Papaderakis, A.; Tsiplakides, D.; Balomenou, S.; Sotiropoulos, S. Electrochemical impedance studies of IrO_2 catalysts for oxygen evolution. *J. Electroanal. Chem.* **2015**, *757*, 216–224. [CrossRef]
33. Teles, J.J.S.; Faria, E.R.; Franco, D.V.; Da Silva, L.M. Inner and Outer Surface Areas, Electrochemical Porosity, and Morphology Factor of Mixed Oxide-Covered Mesh Electrodes with a Nominal Composition of MOME-$Sn_{0.5}Ir_xRu_{(0.5-x)}O_2$. *Int. J. Electrochem. Sci.* **2017**, *12*, 1755–1773. [CrossRef]
34. De Pauli, C.P.; Trassati, S. Electrochemical surface characterization of IrO_2 + SnO_2 mixed oxide electrocatalysts. *J. Electroanal. Chem.* **1995**, *396*, 161–168. [CrossRef]

35. Cherevko, S.; Reier, T.; Zeradjanin, A.R.; Pawolek, Z.; Strasser, P.; Mayrhofer, K.J.J. Stability of nanostructured iridium oxide electrocatalysts during oxygen evolution reaction in acidic environment. *Electrochem. Commun.* **2014**, *48*, 81–85. [CrossRef]
36. Ten Kortenaar, M.V.; Vente, J.F.; Ijdo, D.J.W.; Müller, S.; Kötz, R. Oxygen evolution and reduction on iridium oxide compounds. *J. Power Sources* **1995**, *56*, 51–60. [CrossRef]
37. Hu, J.-M.; Zhang, J.-Q. Microstructure, electrochemical surface and electrocatalytic properties of IrO_2 + Ta_2O_5 oxide electrodes. *J. Mater. Sci.* **2003**, *36*, 705–712. [CrossRef]